Article

Study on nanoscale mechanical properties and fractal characteristics of different mineral regions in shale based on atomic force microscopy experiments

Zhangping Yan[1], Hong Yin[1,*], Wenlong Yu[2], Xin Ning[1], Weipeng Ruan[1], Kaixing Liu[1], Xin Tang[1]

[1] School of Civil Engineering, Chongqing Three Gorges University, Chongqing 404199, China
[2] Chongqing Dazu District Planning and Natural Resources Bureau, Chongqing 404199, China

* Correspondence: 15111846767@163.com

Abstract: This paper studies the micro-heterogeneity and mechanical properties of Lianggaoshan Formation shale in eastern Sichuan, China, so as to explore its influencing factors. The morphology, mechanical parameters, and fractal dimension of different mineral regions were quantitatively analyzed by atomic force microscopy, optical microscopy, and energy dispersive X-ray spectroscopy. The results show that the surface roughness and root mean square roughness of pyrite, quartz, and clay increase in turn. The surface roughness values are 30.33 nm, 37.15 nm, and 48.15 nm, respectively. The square roughness values are 34.56 nm, 41.38 nm, and 54.88 nm, respectively. The elastic modulus range of pyrite, quartz, and clay decreased from 40.85 GPa to 3.59 GPa, while the range of deformation, cohesion, and dissipation energy increased gradually. The fractal dimension value gradually increased from 2.133 to 2.273, indicating that the mineral composition significantly affected the fractal characteristics. A strong correlation of R^2 greater than 0.9 was found between fractal dimension and mechanical parameters, with fractal dimension negatively correlated with Young's modulus and positively correlated with adhesive force, dissipated energy, and deformation. It provides data and theoretical support for geotechnical engineering and shale oil exploration and development technology.

Keywords: Rock mechanics; mineralogy; shale; atomic force microscope; fractal dimension

1. Introduction

Rocks are typical heterogeneous materials that usually contain multiphase minerals and a large number of microscopic pore structures, exhibiting multiscale characteristics. The mechanical properties of different minerals vary significantly, and the microscopic mechanical properties of each component directly control the macroscopic mechanical behavior of the rock (Zhu and Shao, 2017; Sevostianov and Vernik, 2021; Gao and Meguid, 2022). Macroscopic rock mechanics tests indicate that the macroscopic mechanical parameters of rocks exhibit considerable dispersion, which may be closely related to the microscopic mineral heterogeneity at different scales. Fractal theory, as a powerful tool for describing complex geometric shapes and self-similar structures, provides a new perspective for in-depth analysis of the complexity of rock microstructures and their influence on mechanical properties. To some extent, the fractal characteristics of rock microstructures, such as the distribution of mineral particles and the morphology of pores, may determine the dispersion and heterogeneity of their mechanical properties. Therefore, analyzing the microscopic mechanical properties of rocks is of great significance for a deeper understanding of their microscopic mechanical behavior, and the introduction of fractal theory will help to more comprehensively reveal the essence of this microscopic mechanical behavior.

Currently, research on the mechanical properties and failure mechanisms of rocks is typically conducted through field coring, followed by uniaxial or triaxial loading tests in the laboratory (Shuai et al., 2024; Liu

and Wen, 2023; Lin et al., 2023; Jing et al., 2023). However, the traditional uniaxial or triaxial tests require a high sample size and integrity, and the existence of weak bedding planes or natural cracks makes it difficult to guarantee the quality of coring. The non-reproducibility of destructive tests further aggravates the data discreteness. (Zhou et al., 2025; Yang et al., 2024). There are two key limitations in current research. First, it is difficult to directly correlate macroscopic mechanical tests with microscopic heterogeneity. Secondly, the existing microscopic characterization techniques, such as SEM, are mostly focused on morphology observation, and lack quantitative in-situ measurement of mechanical parameters.

Atomic force microscopy (AFM) has been widely used in the study of porous media due to its high-resolution morphological characterization and quantitative mechanical analysis capabilities. (Li, 2025; Saeedi, 2024; Yu, 2024; Choi et al., 2024; Campbell et al., 2025; Li et al., 2024; Nishizawa et al., 2024). Currently, this method has been used to study the nanoscale mechanical properties of porous media and has been applied in fields such as civil engineering and petroleum (Xie and Li, 2024; Zhang et al., 2020; Wang and Liu, 2017; Zhang et al., 2022; Lu et al., 2022; Li et al., 2020). Xie and Li (2024) conducted research and analysis on the microstructure and mechanical properties of coal samples using AFM. Zhang et al. (2020) tested the surface morphology and mechanical behavior of asphalt with different aging times using the PeakForce Tapping technique under the QNM (PF-QNM) mode, obtaining two-dimensional and three-dimensional morphological maps and mechanical behavior parameters of asphalt samples. Wang and Liu (2017) investigated the effects of long-term aging on SBS modified asphalt and base asphalt using AFM. Zhang et al. (2022) studied the relationship between the chemical composition and mechanical properties of asphalt binders using AFM. Lu et al. (2022) researched pore structure, mechanical properties, and wettability (both macroscopic and microscopic contact angles) using nanoscale droplet vapor condensation measurements and AFM. Li et al. (2020) conducted nanoscale detection studies on pore distribution and mechanical properties of coal using SEM and AFM. Although the Peak Force Tapping mode of atomic force microscopy has been widely applied to characterize the nanoscale mechanical properties of porous media in other fields, there are few applications in the characterization of the nanoscale mechanical properties of shale.

Most of the existing studies regard shale as a homogeneous body, ignoring the nano-micromechanical differences of different mineral components (such as clay, quartz, and pyrite). The application of AFM peak force tapping mode (PeakForce Tapping) in the shale field has not been systematized, especially the lack of collaborative analysis with fractal theory. In view of this, the author combined AFM PeakForce Tapping, EDS, and an optical microscope to realize the simultaneous analysis of shale mineral composition identification, morphology characterization, and mechanical parameter measurement. The quantitative relationship between microstructure inhomogeneity

and mechanical properties was established by calculating the fractal dimension of different mineral regions. The nano-scale viscoelastic response of clay minerals in shale is focused on filling the gap in the existing AFM technology in the mechanical characterization of layered silicate minerals.

2. Determination principle of nano-micro scale mechanical properties

2.1 Testing instruments and working principles

Atomic Force Microscopy (AFM) is a type of scanning force microscopy characterized by the detection of interactions between a probe and a sample. In this study, a Bruker Dimension Icon AFM equipped with a Nanoscope V controller and Nanoscope software was used. Its basic working principle involves an elastic cantilever beam, one end of which is fixed while the other end has a tiny tip. As the tip scans the sample, the interaction forces (attractive or repulsive) between the tip and the sample, which are related to their distance, cause the cantilever beam to deform. Simultaneously, a laser beam emitted from a laser source strikes the back of the cantilever beam, which reflects the laser beam onto a photodetector. The signal is input into a control box, where it is processed by software and hardware, allowing for the acquisition of information about the sample's surface morphology or other surface properties. AFM not only reflects the mechanical properties of the measurement system but also provides real-time imaging due to its unique spatial resolution, thus offering more information. There are several basic imaging modes in AFM: tapping mode, contact mode, non-contact mode, torsional resonance mode, and Peak Force Tapping mode (PF-QNM).

In this experiment, the Peak Force Tapping mode of AFM was employed, which allows for the acquisition of quantitative nanoscale mechanical properties of the sample while obtaining its morphology, presenting the measurement results in real-time images (Garcia, 2020; Collinson et al., 2021; Farokh and Passian, 2023; Lou et al., 2023; Penedo et al., 2021; Wei et al., 2024; Tang, 2020).

As shown in Fig. 1(a), the interaction process between the probe and the sample during a Peak Force Tapping cycle is illustrated. The process from A to B to C represents the probe approaching the sample, while C to D to E depicts the probe interacting with the sample and then leaving the sample surface. The segments A to B to C to D to E in Fig. 1(a) correspond to the approach and retraction curves in Fig. 1(b). At position A, when the probe is far from the sample, an attractive force develops as the distance decreases, reaching position B. The probe continues to approach the sample, and at position C, the sample undergoes a certain amount of deformation, while the applied stress gradually increases until it reaches the set peak force. Once the peak stress is reached, the peak stress decreases, and the probe begins to leave the sample. When leaving the sample surface, adhesion occurs due to the attractive forces between the probe atoms and the sample, which occurs at position D. After the adhesion process ends, the probe returns to its initial
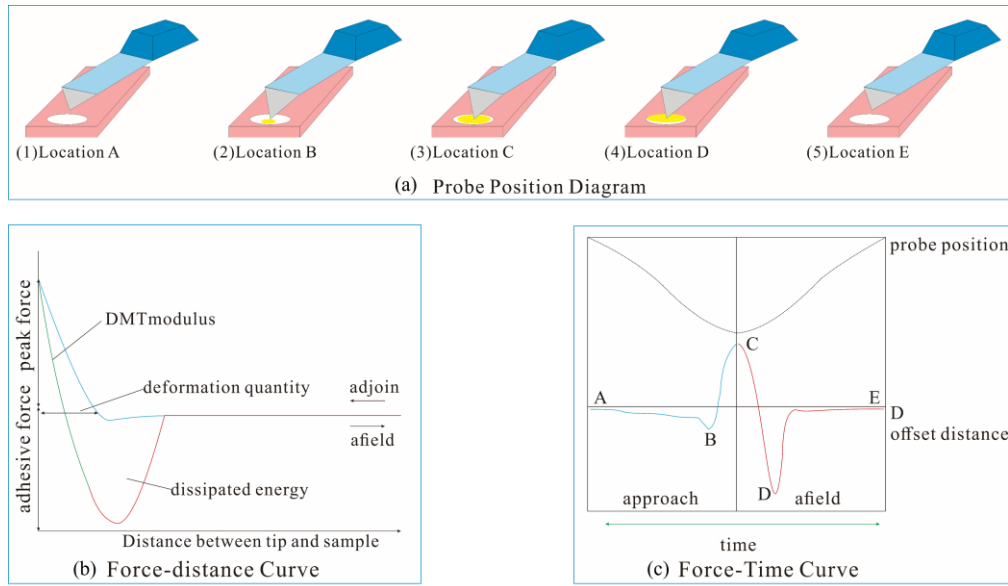
Fig. 1. Test equipment and principle.

position at E. By calibrating the settings of the scanner, the AFM system can convert the force-time curve (Fig. 1(b)) into a force-distance curve (Fig. 1(c)).

The resulting force-distance curve includes the approach force-distance curve and the retraction force-distance curve. A detailed analysis of the force-distance curve allows for the determination of properties such as the Young's modulus, adhesive force, deformation amount, and dissipated energy of the sample (Fig. 1(c)).

2.2 Testing mechanical parameters

(1) Roughness

Calculating the three-dimensional roughness of the sample can evaluate the surface morphological characteristics of the material. Two important parameters are selected for analyzing and processing the experimental results: the surface arithmetic mean roughness (R_a) and the surface root mean square roughness (R_q). Here, R_a represents the average distance between the baseline and the surface, while R_q indicates the variance of the surface morphology (Wu et al., 2020; Beretta et al., 2020; Khanna et al., 2021). The formulas (1), (2), and (3) can be obtained as follows:

$$R_a = \frac{1}{N_x N_y} \sum_{i=1}^{N_x} \sum_{j=1}^{N_y} | z(i,j) - z_m | \quad (1)$$

$$R_q = \sqrt{\frac{1}{N_x N_y} \sum_{i=1}^{N_x} \sum_{j=1}^{N_y} (z(i,j) - z_m)^2} \quad (2)$$

$$z_m = \frac{1}{N_x N_y} \sum_{i=1}^{N_x} \sum_{j=1}^{N_y} z(i,j) \quad (3)$$

In the formulas: N_x and N_y represent the number of scan points along the x-axis and y-axis, respectively；$z(i,j)$ is the height at the (i,j) measurement point; and z_m is the average height of all measurement points.

(2) Young's Modulus

During the testing process, a Poisson's ratio of 0.3 is set (Li et al., 2025; Oliver et al., 1992; Oliver et al.,

2004), allowing for the analysis of the DMT modulus value of the sample. The calculation formulas are given in equations (4) and (5):

$$F - F_{adh} = \frac{4}{3} E \sqrt{R d^3} \quad (4)$$

In the equations: F represents the force exerted by the probe on the sample; F_{adh} is the adhesion force generated at the moment the probe moves away from the sample; R is the radius at the tip of the probe; d is the deformation of the sample; E is the DMT modulus of the sample.

$$\frac{1}{E} = \frac{1-v_s^2}{E_s} + \frac{1-v_{tip}^2}{E_{tip}} \quad (5)$$

In the equations, v_s and v_{tip} represent the Poisson's ratios of the standard sample and the probe, respectively; E_{tip} is the elastic modulus of the probe, which is generally considered to be very large, and when included in the denominator, it is regarded as negligible in the polynomial equation; E_s is the actual modulus of the sample.

(3) Adhesion Force

When the probe is about to leave the surface of the sample, an adhesion force is generated. The method for calculating the adhesion force based on the DMT model chosen in this study is shown in equation (6):

$$F_a = 2\pi R \omega \quad (6)$$

In this equation, F_a represents the adhesion force; R is the contact radius; ω is the work of adhesion.

(4) Fractal Dimension

Fractal Dimension (D) is a mathematical tool used to quantify the complexity and irregularity of an object. In AFM image analysis, fractal dimension can be used to describe the roughness, complexity, and self-similarity of a sample's surface.

The methods for calculating the fractal dimension D of an image mainly include the box-counting method, methods based on fractional Brownian random field models, and the box dimension method.

Sustain. Earth Resour. Commun. 2025, 1(1): 3-16

6

These methods differ in precision and complexity. The box dimension method is more accessible for programmatic design and calculation, thus receiving widespread attention from both theorists and practitioners (Teng et al., 2025; Liu et al., 2025). The box dimension method involves placing the fractal object on a uniformly divided grid and calculating the minimum number of boxes needed to completely cover the pore defects. Subsequently, by refining the grid, the total number of boxes required at different box scales can be obtained. A log-log plot of the box edge length (h) versus the total number of boxes (N) is created, and the fractal dimension D is defined as the negative slope of the curve, as shown in formulas (7) and (8):

$$D = -\lim_{h \to 0} \frac{\log N}{\log r} = \lim_{h \to 0} \frac{\log N}{\log h} \quad (7)$$

$$r = 1/h \quad (8)$$

3. Determination experiments for nanoscale mechanical properties of shale
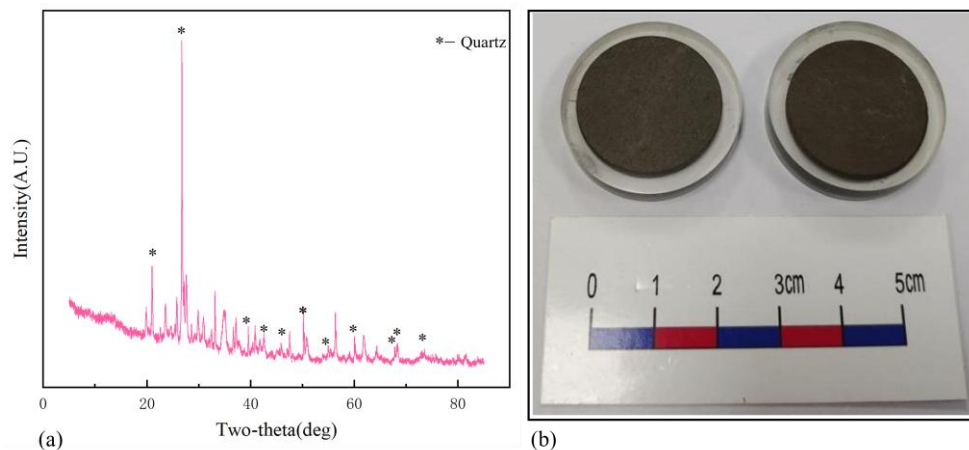
3.1 Sample preparation

The samples in this study were selected from the field outcrops of the Lianggaoshan Formation shale in eastern Sichuan, with an average organic carbon content (TOC) of about 1.03%. According to the X-ray diffraction experiment (XRD), it is shown that the quartz brittle minerals are more abundant in the shale samples, as shown in Fig. 2(a). Since Atomic Force Microscopy (AFM) measures at the nanometer scale, the testing surface must be extremely smooth. Therefore, a stepped polishing method was used to prepare the samples. An ultrasonic cleaning device was employed to remove dust and impurities from the sample surface to ensure the accuracy of subsequent experiments.

High-precision cutting tools were used to cut the shale samples into small pieces with a thickness of 1-3 millimeters, ensuring a flat cutting surface. The samples were polished stepwise with sandpaper of varying fineness and polishing solution to achieve a smooth and uniform surface, ensuring measurement accuracy during AFM testing. The polished samples are shown in Fig. 2(b). This study prepared two shale samples, labeled YY-1 and YY-2, to investigate the differences between the samples in the AFM experiments.

3.2 Selection of experimental areas

Shale is rich in various mineral components. To accurately assess the mechanical properties of different mineral regions within the shale, it is necessary to determine the mineral composition around the scanning points before conducting AFM tests. Selected through an optical microscope based on characteristics such as mineral color, luster, and crystal form, the regions are subsequently analyzed using an X-ray energy dispersive spectroscopy (EDS) system. Ultimately, shale areas rich in pyrite, quartz, and clay matrix are chosen for AFM scanning, as shown in Fig. 3, thereby supporting the study of the mechanical properties of different minerals in shale.

Fig. 2. (a) X-ray diffraction (XRD) and (b) Sample preparation.
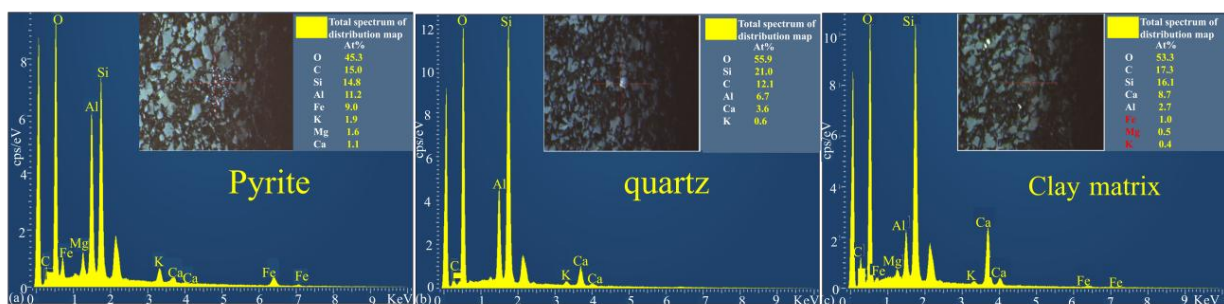
Fig. 3. Selection of Shale Experimental Areas.

3.3 Experimental parameter settings

To accurately determine the elastic properties of materials using AFM, a suitable probe is required. In this study, the RTESPA-525 probe model is selected, as its tip provides sufficient hardness to avoid significant deformation of the probe itself. This probe is suitable for measuring materials with an elastic modulus range of 0 GPa to 100 GPa, made of single-crystal silicon, with an elastic constant of 200 N·m^{-1}, a resonance frequency of 525 Hz, a tip height ranging from 10 to 15 μm, and a tip radius from 8 to 12 nm. Before each test, a relative calibration method is necessary to calibrate the sensitivity of the AFM photodetector and the probe parameters (tip radius and cantilever spring constant).

First, the cantilever deflection sensitivity needs to be calibrated by obtaining a standard force-displacement curve on a clean glass slide and then calculating the slope of this curve. Next, the cantilever spring constant is calibrated using the thermal noise method to obtain the corrected cantilever spring constant. Finally, the probe diameter is calibrated by conducting tests on materials with known elastic moduli. By adjusting the probe diameter, the measured reduced elastic modulus is made approximately equal to the material's elastic modulus, determining the equivalent diameter of the probe.

During the testing process, the scan range is set to 30 μm × 30 μm, with an image resolution of 256 pixels × 256 pixels, a scan frequency of 1.98 Hz, a peak force of 300 nN, an amplitude of 40 nm, and a peak force frequency of 2000 Hz. Data and spectra are processed using the open-source software Gwyddion 2.53 and NanoScope Analysis 3.00. The measured morphological data undergo planar processing to showcase the three-dimensional details of the morphology. The mechanical parameters and spectra are presented as raw measured values without any special processing.

4. Experimental results analysis

4.1 Nanoscale morphology of shale

From the realistic 3D morphological features of the samples observed using AFM (Fig. 4 and 5), it can be seen that at the nanoscale, the six tested surfaces are not absolutely smooth but exhibit clear peaks and valleys. The R_a for the pyrite region of YY-1 is 37.05 nm, and the R_q is 39.67 nm, while for the pyrite region of YY-2, R_a is 30.33 nm and R_q is 34.56 nm. For the quartz region of YY-1, R_a is 38.95 nm and R_q is 45.14 nm, while for the quartz region of YY-2, R_a is 37.15 nm and R_q is 41.38 nm. In the clay matrix region, YY-1 has R_a of 48.75 nm and R_q of 55.96 nm, while YY-2 has R_a of 48.19 nm and R_q of 54.88 nm. Comparing the R_a and R_q values of different regions of shale in YY-1 and YY-2, it is found that the roughness of the surface of the clay matrix, quartz, and pyrite regions decreases in turn.

Through a two-dimensional profile analysis of the diagonal lines at the test positions, it can be seen that the surface of the tested samples fluctuates, indicating that the shale surface is filled with nanoscale pores of different shapes and sizes. This result aligns with current research findings, which state that shale is a porous medium rich in nanoscale pores, and distinct differences exist across various shale surfaces. The roughness of the rock samples is also related to the degree of polishing; better polishing results in less adhering dirt, and consequently, a smaller extent of surface fluctuation.

4.2 Nanoscale mechanical parameters of shale

(1) Young's Modulus and Deformation Amount

It was found that the elastic modulus cloud map and the strain cloud map exhibit good consistency (Fig. 6 and 7), indicating that the surface morphological characteristics have a certain impact on the elastic modulus of the samples.
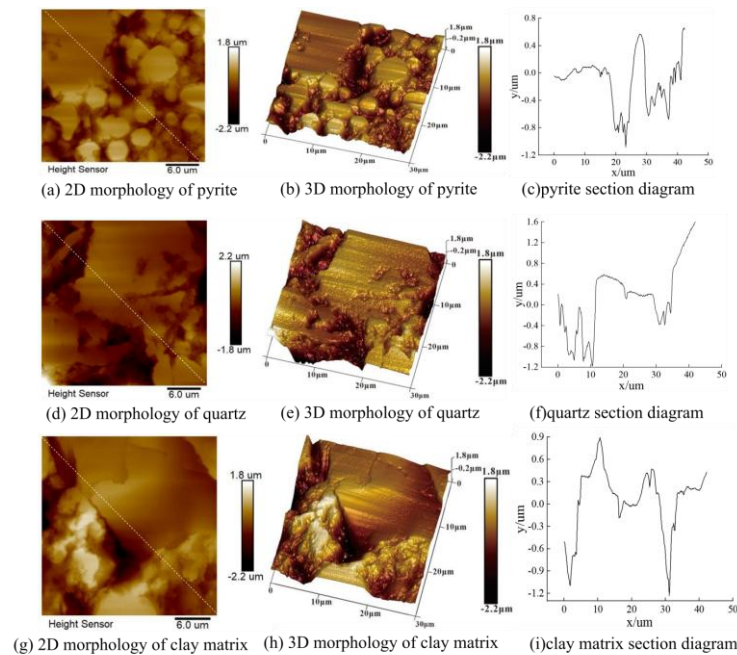
A comparison of the elastic modulus and deformation in different mineral regions of the shale revealed that for YY-1, the average elastic modulus for pyrite, quartz, and the clay matrix in the test area is 40.85 GPa, 29.17 GPa, and 3.009 GPa, respectively. The average deformation values for pyrite, quartz, and the clay matrix in YY-1 are 3.43 nm, 4.14 nm, and 5.79 nm, respectively. For YY-2, the average elastic modulus for pyrite, quartz, and the clay matrix in the test area are 50.03 GPa, 38.39 GPa, and 3.59 GPa, respectively, while the average deformation values for these regions are 3.03 nm, 3.98 nm, and 5.64 nm, respectively.

The comparison shows that pyrite and quartz have larger elastic moduli, while the clay matrix has a smaller elastic modulus. The deformation of pyrite and quartz is relatively small, while the deformation in the clay matrix is larger. Based on this, we compare the deformation and Young's modulus of the experimental results and find that the mechanical properties of shale have a strong correlation with material properties. At the same time, the atomic force microscope can record the force-distance line and Young's modulus at the same time, and realize the real-time correlation of micromechanics, so as to provide reliability support for the multi-directional application of test data.
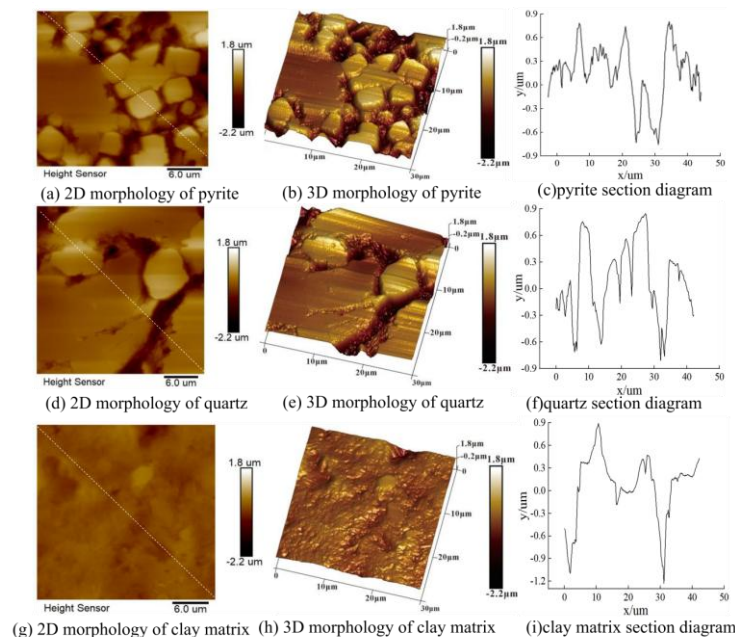
Analysis of the results indicates that there are significant differences in the mechanical properties and deformation amounts of different mineral regions in the shale, but these differences have certain correlations: greater deformation in mineral-rich areas tends to correlate with a smaller elastic modulus. Literature (Wang, 2021; Volkov, 2020; De Souza et al., 2021; Yang et al., 2024) indicates that the elastic modulus values obtained from AFM experiments are higher than those from traditional macromechanical testing. This discrepancy can be attributed to two main factors.

First, the presence of microcracks in the samples affects traditional macro test results, whereas AFM works on a micro-nano scale, where the influence of microcracks can be ignored. Second, the samples exhibit viscoelasticity, and the adhesion force between the AFM probe and the sample can affect the elastic modulus to some extent, an aspect not considered in macro testing.

(a) 2D morphology of pyrite   (b) 3D morphology of pyrite   (c) pyrite section diagram

(d) 2D morphology of quartz   (e) 3D morphology of quartz   (f) quartz section diagram

(g) 2D morphology of clay matrix   (h) 3D morphology of clay matrix   (i) clay matrix section diagram

Fig. 4. Nanoscale Morphological Characteristics of Shale Sample YY-1.

(a) 2D morphology of pyrite   (b) 3D morphology of pyrite   (c) pyrite section diagram

(d) 2D morphology of quartz   (e) 3D morphology of quartz   (f) quartz section diagram

(g) 2D morphology of clay matrix   (h) 3D morphology of clay matrix   (i) clay matrix section diagram

**Fig. 5.** Nanoscale Morphological Characteristics of Shale Sample YY-2.

(2) Adhesion Force

Analysis reveals significant differences in the adhesion forces of different mineral regions in the shale, as shown in Fig. 8 and 9. For YY-1, the average adhesion forces in the test regions for pyrite, quartz, and the clay matrix are 136.369 nN, 167.802 nN, and 232.081 nN, respectively. For YY-2, the average adhesion forces in the test regions for pyrite, quartz, and the clay matrix are 119.153 nN, 145.6 nN, and 202.5 nN, respectively.
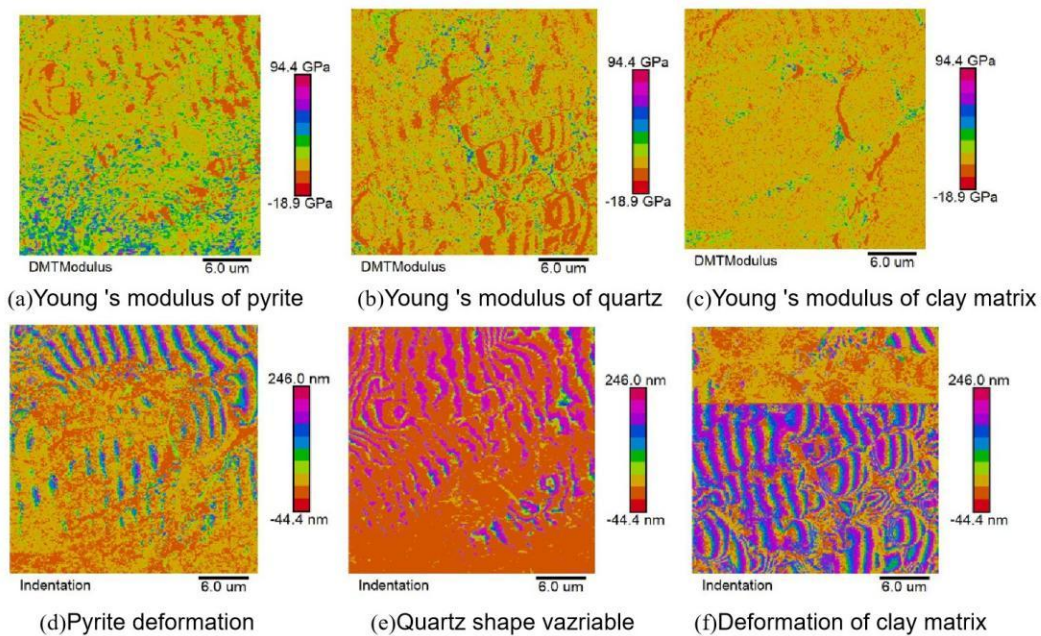
The test results indicate that while shale exhibits homogeneity at the matrix scale, significant heterogeneity remains at the nanoscale, possibly due to differing response mechanisms to the sedimentary environment during the formation of the shale.
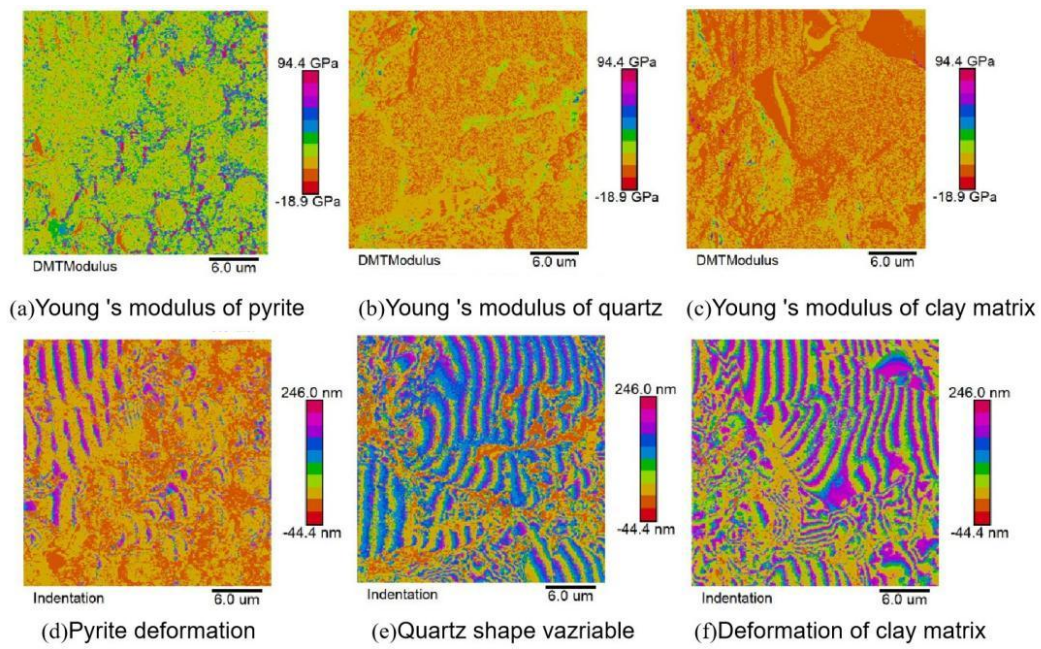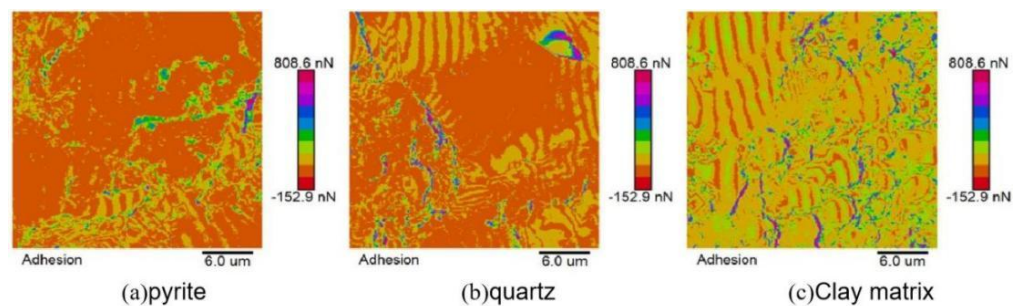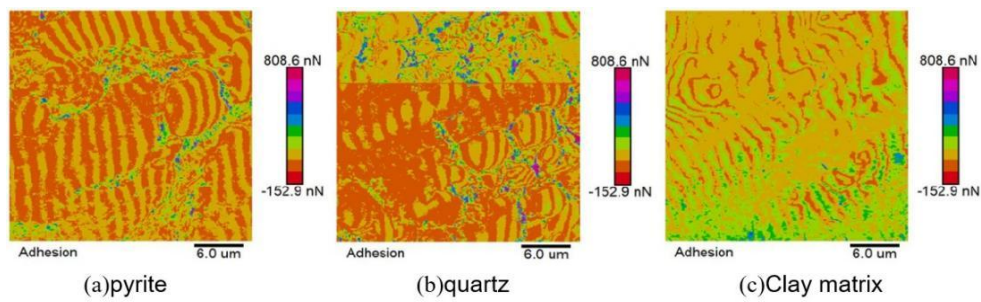
Fig. 6. Elastic Modulus and Strain of Shale Sample YY-1.

Fig. 7. Elastic Modulus and Strain of Shale Sample YY-2.

**Fig. 8.** Adhesion Force of Shale Sample YY-1.

**Fig. 9.** Adhesion Force of Shale Sample YY-2.

(3) Dissipated Energy

Dissipated energy refers to the energy consumed by the shale during loading and unloading processes. This parameter reflects the development of internal micro-defects and the strength of the shale, which is closely related to its damage and fracture characteristics (Tang, 2020). There are also significant differences in dissipated energy among different shale samples (as shown in Fig. 10 and 11). For YY-1, the average dissipated energy in the test regions for pyrite, quartz, and the clay matrix is 51.25 KeV, 90.06 KeV, and 132.35 KeV, respectively. For YY-2, the average dissipated energy in the test regions for pyrite, quartz,

and the clay matrix is 45.48 KeV, 78.06 KeV, and 100.35 KeV, respectively.

The dissipated energy is primarily caused by plastic deformation of the samples and is related to adhesion force and maximum deformation. Thus, the greater the adhesion force and deformation, the larger the dissipated energy. As stated earlier, the average adhesion force and deformation of the different minerals in the test region for YY-1 are higher than those for YY-2. Therefore, the dissipated energy for different minerals in YY-1 is also higher than that for YY-2, further confirming the accuracy and reliability of the experiment.
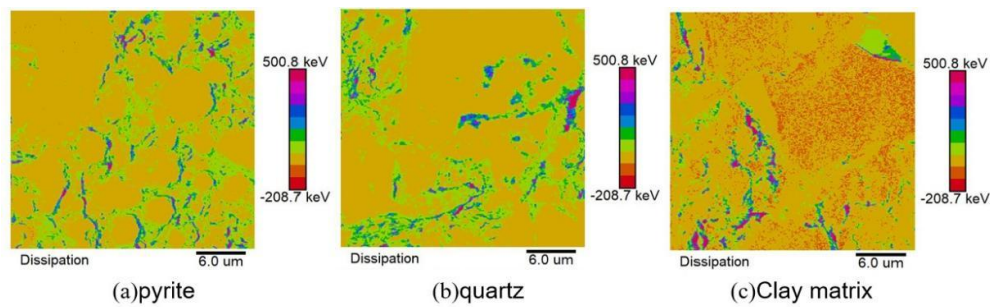
**Fig. 10.** Dissipated Energy of Shale Sample YY-1.
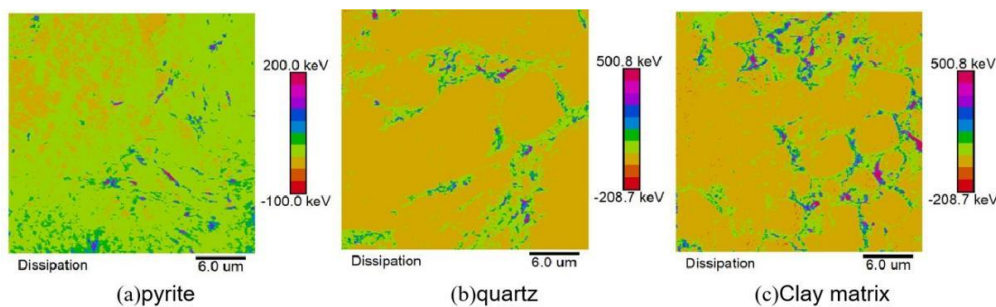
Fig. 11. Dissipated Energy of Shale Sample YY-2.

4.3 *Fractal dimension of shale*

The fractal dimensions of different mineral regions in various shales were calculated using the box-counting method (Table 1 and Fig. 12). The fitting coefficients of the fractal dimensions (R^2) are all greater than 0.9, indicating that the shales of the Lianggaoshan Formation in the eastern Sichuan region conform to fractal laws and exhibit self-similarity. Among them, the fractal dimension D of YY-1 shale ranges from 2.161 to 2.273, with an average of 2.216, while the fractal dimension D of YY-2 shale ranges from 2.133 to 2.254, with an average of 2.187. The fractal dimension D of the pyrite region in the test area ranges from

2.133 to 2.161, with an average of 2.147. The fractal dimension D of the quartz region in the test area ranges from 2.174 to 2.213, with an average of 2.194, and the fractal dimension D of the clay matrix region in the test area ranges from 2.254 to 2.273, with an average of 2.264. Comparatively, the fractal dimension D of YY-1 shale is greater than that of YY-2 shale. The fractal dimensions D in shale rich in different mineral regions are not the same; the fractal dimension D is greatest in shale rich in clay minerals and smallest in shale rich in pyrite, indicating that mineral composition affects the fractal dimension D.
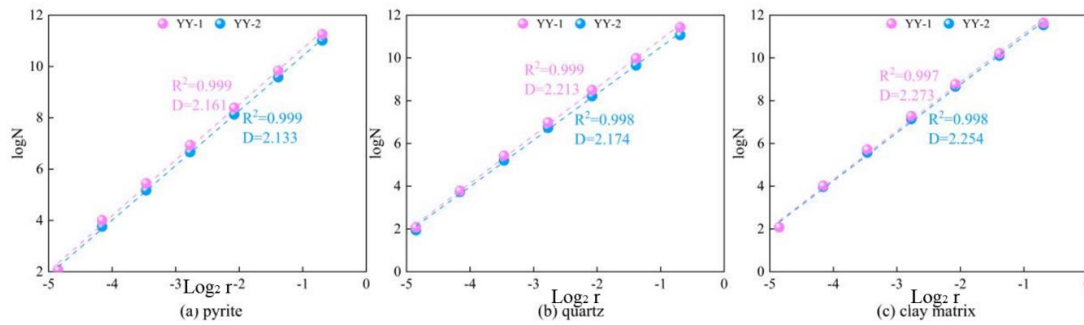
Fig. 12. Fractal Dimension of Shale.

Table 1. Shale fractal dimension results.

Sample	Mineral Area	Fitting Value (R^2)	Fractal Dimension	Mean Value
	Pyrite	0.999	2.161	
YY-1	Quartz	0.999	2.213	2.216
	Clay matrix	0.997	2.273	
	Pyrite	0.999	2.133	
YY-1	Quartz	0.998	2.174	2.187
	Clay matrix	0.998	2.254	

5. Discussion

Through X-ray diffraction (XRD) analysis of different samples (as shown in Table 2), it was found that the proportions of quartz, feldspar, carbonate, other, and clay minerals in YY-1 shale were 30.1%, 4.4%, 0%, 5.4% and 60.1%, respectively. The proportions of quartz, feldspar, carbonate, other, and clay minerals in YY-2 shale were 40.9%, 7.1%, 0%, 0.6% and 51.4%, respectively.

Table 2. Different shale mineral composition

Sample	Quartz (%)	Feldspar (%)	Carbonate (%)	Other (%)	Clay Mineral (%)
YY-1	30.1	4.4	0	5.4	60.1
YY-2	40.9	7.1	0	0.6	51.4

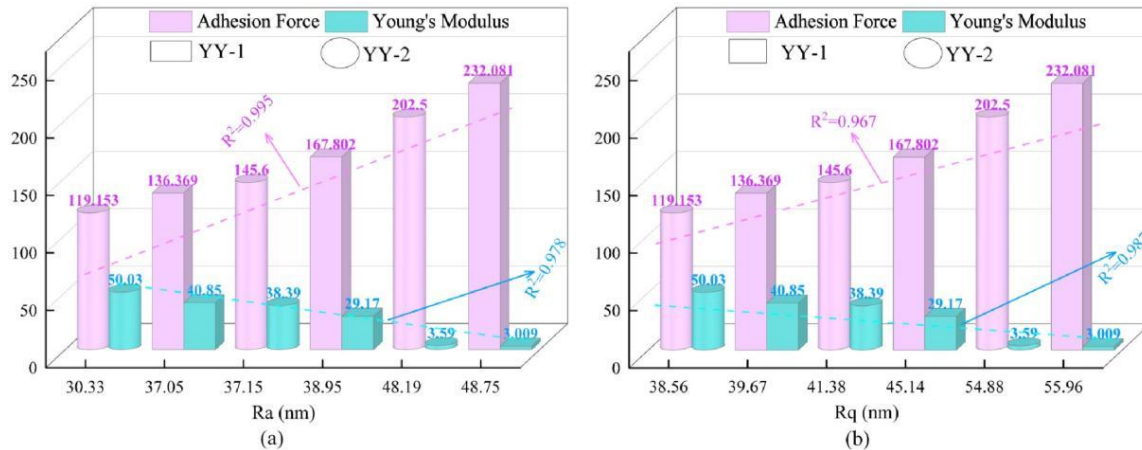### 5.1 The relationship between roughness, adhesion force, and Young's modulus

By analyzing the fitting relationship between shale roughness parameters (R_a and R_q) and Young's modulus (Fig. 13), it can be observed that R_a and R_q exhibit a negative correlation with Young's modulus, with fitting coefficients R^2 of 0.978 and 0.987, respectively. This significant linear relationship indicates that Young's modulus decreases as R_a and R_q increase. From a microscopic perspective, changes in roughness imply alterations in the nanoscale morphology and pore structure of the shale's surface. When subjected to external forces, these pores and defects become stress concentration points, making the shale more susceptible to deformation and failure, thereby reducing the overall stiffness of the shale, which means that Young's modulus decreases. Zhang et al. (2022) found through atomic force microscopy studies on slate that nanoscale surface morphology affects the mechanical properties of slate; changes in roughness measured by atomic force microscopy can lead to variations in Young's modulus.

By analyzing the fitting relationship between the adhesion force of shale samples and roughness parameters (R_a and R_q) (Fig. 13), it is evident that R_a and R_q exhibit a positive correlation with adhesion force, with fitting coefficients R^2 of 0.995 and 0.967, respectively. This significant linear relationship indicates that adhesion force decreases as R_a and R_q increase. Generally,

increased roughness of the shale enhances the actual contact area between the shale and other substances. According to contact mechanics theory, the increase in contact area provides more points of interaction between the two, resulting in a tendency for adhesion force to increase. On a microscopic level, the unevenness of a rough surface allows for more thorough contact between the shale and other materials, thereby strengthening the adhesion effect between them (Bai,

2022). Changes in roughness also affect the distribution of surface energy on the shale. Rough surfaces, with more microscopic structures such as pores, protrusions, and depressions, lead to a more complex distribution of surface energy. A higher surface energy promotes stronger adsorption of the shale onto other materials, thereby increasing adhesion force (Kang, 2024).

Fig. 13. Fitting Relationship of Roughness with Adhesion Force and Young's Modulus.

5.2 The relationship between fractal dimension, adhesion force, and Young's modulus

The traditional roughness parameters only quantify the arithmetic mean of surface undulation, while the fractal dimension (D) describes the geometric complexity and multi-scale self-similarity of surface texture, which is more directly related to the microstructure and macroscopic properties. The fractal dimension, as a parameter that effectively characterizes the roughness and complexity of shale surfaces, has a crucial impact on adhesion force and Young's modulus (Liu et al. 2025). A detailed analysis of the fitting relationship between fractal dimension D and adhesion force and Young's modulus (Fig. 14) reveals a significant positive correlation between fractal dimension D and adhesion force, with a fitting coefficient R^2 of 0.977. This strongly indicates a close and stable linear relationship, meaning that as the fractal dimension increases, the adhesion force also increases 0Kang et al., 2024). However, comparisons with previous studies show that a higher fractal dimension D is associated with increased surface roughness, which reduces the actual effective contact area and could theoretically lead to a decrease in adhesion force. Yet, the results of this study contradict this; the discrepancy may arise from differences in testing methods and the complexity of microstructures, among other factors.

On the other hand, the fractal dimension D shows a negative correlation with Young's modulus, with a fitting coefficient R^2 of 0.966, indicating a significant linear relationship. This means that as the fractal dimension increases, Young's modulus decreases. Shales with a higher fractal dimension typically have a more complex microstructure that includes more micro-cracks, pores, and irregular crystal structures.

These microstructural characteristics can lead to uneven stress distribution within the shale. When subjected to external forces, stress may not be uniformly transmitted but is more likely to concentrate in defects such as micro-cracks and pores, making the shale more susceptible to deformation, ultimately reflected as a reduction in Young's modulus.

The strong linear correlation between fractal dimension (D) and elastic modulus (E) ($R^2 = 0.966$) indicates that there is a robust statistical correlation between them, but this does not mean that there is a one-way causal relationship. On the contrary, this correlation is likely to be due to the combined effect of sample microstructure heterogeneity on the two. The fractal dimension can quantify the irregularity and complexity of the pore/particle structure inside the sample (Zhang et al., 2020). The higher the fractal dimension, the more tortuous the pore network and the more uneven the particle accumulation. In the process of mechanical loading, this kind of structure can effectively alleviate the stress concentration due to the uniform distribution of contact points between particles, thus improving the elastic modulus and strength.

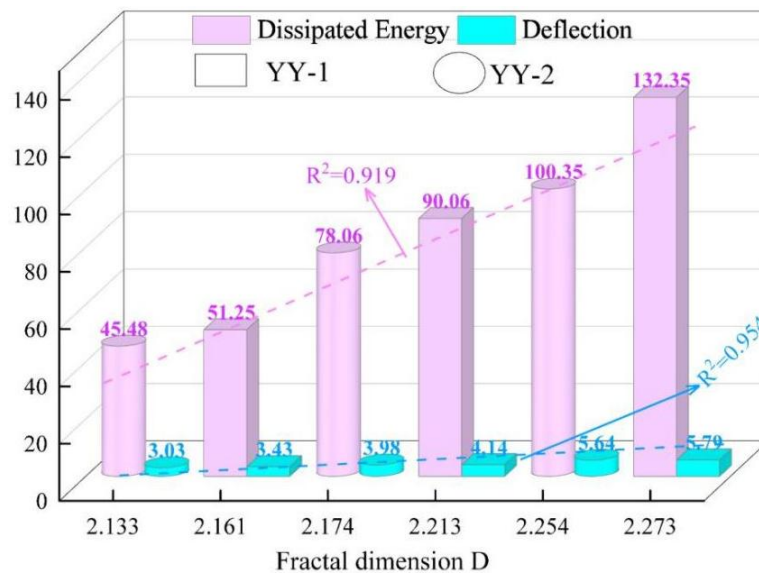### 5.3 The relationship between fractal dimension, deformation amount, and dissipated energy

During the stress process, the deformation behavior of shale and the energy dissipation mechanism are closely linked to its microstructure, with fractal dimension being a key parameter to accurately describe this microstructural complexity. Analyzing the fitting relationship between fractal dimension D and dissipated energy and deformation amount (Fig. 15) shows that as the fractal dimension D increases from 2.133 to 2.273, the dissipated energy significantly increases from 45.48 KeV to 132.35 KeV, and the deformation

amount also increases from 3.03 nm to 5.79 nm. This clearly indicates a significant positive correlation between fractal dimension D, dissipated energy, and deformation amount, with fitting coefficients R^2 of 0.919 for dissipated energy and R^2 of 0.954 for deformation amount, both showing strong linear relationships.
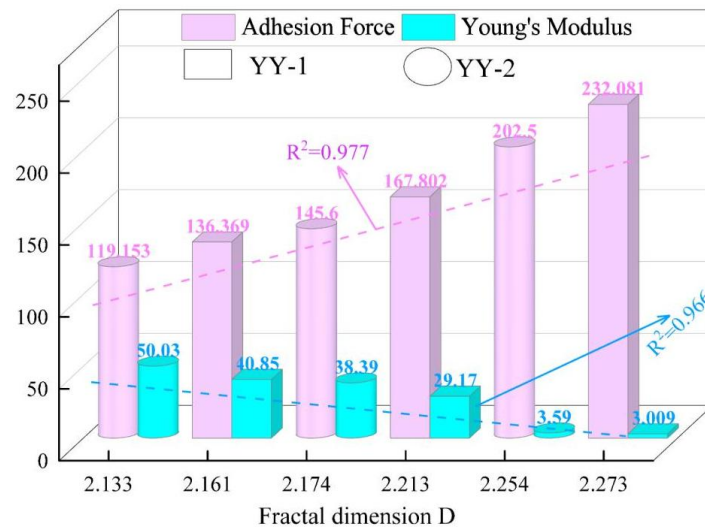
Fig. 14. Fitting Relationship of Fractal Dimension D with Adhesion Force and Young's Modulus.

Fig. 15. Fitting Relationship of Fractal Dimension D with Deformation Amount and Dissipated Energy.

Further investigation into the underlying reasons reveals that a higher fractal dimension indicates greater surface roughness and increased complexity and irregularity of the microstructure. When shale is subjected to external forces, this complex microstructure causes the stress transfer paths within the material to become highly convoluted and intricate, resulting in very uneven stress distribution. This uneven distribution is more likely to trigger localized stress concentrations, leading to deformation in those areas first, which in turn induces deformation in the surrounding areas, ultimately resulting in a larger overall deformation of the shale. Additionally, during the deformation process, the complexity of the microstructure increases the pathways for energy dissipation. For instance, changes within the microstructure, such as the propagation of micro-

cracks, slip between grains, and dislocation movement, consume energy. Furthermore, the complex microstructure may also facilitate the transfer and transformation of energy across different scales, such as from macro elastic deformation energy to micro thermal energy and acoustic energy. These factors collectively contribute to significant energy dissipation in the shale (Wang et al., 2023; Zhuo, 2024).

6. Conclusions

The research on the microscopic mineral mechanical properties of shale in this paper is of great significance for the description of reservoir characteristics and the study of macroscopic mechanical properties. The mineral composition and surface morphology of shale directly affect its macroscopic

mechanical properties, and explain the heterogeneity of shale macroscopic mechanics. Based on the study of microscopic mechanical parameters, it can provide parameters for reservoir anisotropy modeling. The main conclusions are as follows :

(1) Using the AFM Peak Force Tapping mode, the R_a values of the pyrite-rich regions in the shale range from 30.33 to 37.05 nm, while the R_q values range from 34.56 to 39.67 nm. In the quartz-rich regions, the R_a values range from 37.15 to 38.95 nm, and the R_q values range from 41.38 to 45.14 nm. For the clay matrix-rich regions, the R_a values range from 48.15 to 48.75 nm, and the R_q values range from 54.88 to 55.96 nm. Comparisons indicate that R_a and R_q are in the order of pyrite < quartz < clay matrix.

(2) The elastic modulus obtained from the AFM experiments for the pyrite, quartz, and clay matrix-rich regions of the shale are found to be between 40.85 to 50.03 GPa, 29.17 to 38.39 GPa, and 3.009 to 3.59 GPa, respectively. The deformation amounts for these regions are between 3.03 to 3.43 nm for pyrite, 3.98 to 4.14 nm for quartz, and 5.64 to 5.79 nm for the clay matrix. It is observed that the elastic modulus follows the order: pyrite > quartz > clay matrix, while the deformation amount follows the order: pyrite < quartz < clay matrix, indicating that a higher elastic modulus corresponds to a smaller deformation amount. The adhesion forces in the pyrite, quartz, and clay matrix-rich regions are between 119.153 to 136.369 nN, 145.6 to 167.802 nN, and 202.5 to 232.081 nN, respectively. The dissipated energies for these regions are from 45.48 to 51.25 KeV, from 78.06 to 90.06 KeV, and from 100.35 to 132.35 KeV, respectively. The adhesion forces exhibit the order: pyrite < quartz < clay matrix, and the dissipated energies follow the same order: pyrite < quartz < clay matrix. Overall, it is found that as the deformation amount increases, both the dissipated energy and adhesion force increase.

(3) The calculated fractal dimension results indicate that the fractal dimension D of YY-1 shale is greater than that of YY-2 shale. The fractal dimension D for the pyrite-rich regions ranges from 2.133 to 2.161, for the quartz-rich regions from 2.174 to 2.213, and for the clay matrix-rich regions from 2.254 to 2.273. It is observed that the fractal dimension D follows the order: pyrite < quartz < clay matrix, indicating that mineral composition affects the fractal dimension D. Furthermore, there is a significant correlation between the fractal dimension and the nanoscale parameters of shale. Specifically, fractal dimension D shows a negative correlation with Young's modulus, while it shows significant positive correlations with adhesion force, dissipated energy, and deformation amount, with fitting coefficients (R^2) exceeding 0.9, demonstrating significant relationships. This indicates that the fractal dimension can serve as an important parameter for evaluating the micro-mechanical and morphological characteristics of shale, which holds great significance for future exploratory development in the study area.

Author Contributions

X.T. and Y.H.: conceptualization, methodology, software; Z.Y.: data curation, writing—original draft preparation; W.Y.: investigation; Y.H.: supervision; X.N.: software, validation; W.Y., X.N., W.R. and K.L.: writing—reviewing and editing. All authors have read and agreed to the published version of the manuscript.

Funding

Data Availability Statement

Not applicable.

Acknowledgement

Conflicts of Interest

The authors declare no conflict of interest.

Use of AI and AI-assisted Technologies

No AI tools were utilized for this paper.

Open Access

Reference

Bai, T., Yang, F., Wang, H., et al. Adhesion forces of shale oil droplet on mica surface with different roughness: An experimental investigation using atomic force microscopy. Energies, 2022, 15(17): 6460.

Beretta, S., Gargourimotlagh M., Foletti S., et al. Fatigue strength assessment of "as built" AlSi10Mg manufactured by SLM with different build orientations. International Journal of Fatigue, 2020, 139: 105737.

Campbell, C. A., Klapetek, P., Šlesinger, R., et al. Fitting the AFM force–distance curves the correct way. Measurement Science and Technology, 2025, 36(1): 015022-015022.

Choi, M., Schoenek, B., Min, G., et al. Correlative SECCM and AFM microscopy study of local electrochemical activity in HOPG. Electrochemical Society Meeting Abstracts, 2024, MA2024-02(56): 3778.

Collinson, D. W., Sheridan, R. J., Palmeri, M. J., et al. Best practices and recommendations for accurate

Sustain. Earth Resour. Commun. 2025, 1(1): 4-17

15

nanomechanical characterization of heterogeneous polymer systems with atomic force microscopy. Progress in Polymer Science, 2021, 119: 101420.

De Souza, F. B., Zheng, C., Chen, S., et al. Near-field infrared microscopy: A novel analytic mapping technique to nanocharacterize calcium silicate-based cement materials. Cement and Concrete Research, 2021, 147: 106525.

Farokh Payam, A., Passian A. Imaging beyond the surface region: Probing hidden materials via atomic force microscopy. Science Advances, 2023, 9(26): eadg8292.

Gao, G., Meguid, M. A. On the role of joint roughness on the micromechanics of rock fracturing process: a numerical study. Acta Geotechnica, 2022, 17(7): 2799-2824.

Garcia, R. Nanomechanical mapping of soft materials with the atomic force microscope: Methods, theory and applications. Chemical Society Reviews, 2020, 49(16): 5850-5884.

Gong, Z., Chen, S., Ishimwe, H., et al. Study on microscale mechanical properties of minerals and organic matter in shale based on atomic force microscopy. AAPG Bulletin 2024; 108 (3): 495-520.

Kang, Y., Ning, Z., Lyu, F., et al. Nanoscale profiling of the relationship between in-situ organic matter roughness, adhesion, and wettability under $ScCO_2$ based on contact mechanics. Fuel, 2024, 362: 130833.

Khanna, N., Shah, P., de Lacalle, L. N. L., et al. In pursuit of sustainable cutting fluid strategy for machining Ti-6Al-4V using life cycle analysis. Sustainable Materials and Technologies, 2021, 29: e00301.

Li, M., Yan, Z., Tang, X. Micro-mechanical characteristics and thermo-mechanical coupling simulation of organic-rich shale after high temperature. Engineering Geology, 2025, 33(2): 491-502.

Oliver, W. C., Pharr, G. M. An improved technique for determining hardness and elastic modulus using load and displacement sensing indentation experiments. Journal of materials research, 1992, 7(6): 1564-1583.

Oliver, W. C., Pharr, G. M. Measurement of hardness and elastic modulus by instrumented indentation: Advances in understanding and refinements to methodology. Journal of materials research, 2004, 19(1): 3-20.

Li, J., Li, Y., Hassani, M. Mechanically driven refractory high entropy alloy coatings: Phase formation and mechanical properties. Surface & Coatings Technology, 2025, 496: 131669-131669.

Li, Y., Pan, J., Wang, H., et al. Microstructural response of coal fracture surface induced by $ScCO_2$ injection measured with AFM. Gas Science and Engineering, 2024, 131205471-205471.

Li, Y., Yang, J., Pan, Z., et al. Nanoscale pore structure and mechanical property analysis of coal: An insight combining AFM and SEM images. Fuel, 2020, 260: 116352.

Lin, Y., Li, C., Zhou, K., et al. A constitutive model study of chemical corrosion sandstone based on support vector machine and artificial bee colony algorithm. Sustainability, 2023, 15(18): 13415.

Liu, K., Sun, J., Wu, H., et al. Shale sample permeability estimation using fractal parameters computed from TransUnet-based SEM image segmentation. Computers and Geosciences, 2025, 194: 105745-105745.

Liu, L., Wen, B. Study on experimental and constitutive model of granite gneiss under hydromechanical properties. Applied Sciences, 2023, 13(22): 12130.

Lou, Z., Zhang, Y., Li, Y., et al. Study on microscopic physical and chemical properties of biomass materials by AFM. Journal of Materials Research and Technology, 2023, 24: 10005-10026.

Lu, Y., Liu, D., Cai, Y., et al. AFM measurement of roughness, adhesive force and wettability in various rank coal samples from Qinshui and Junggar basin, China. Fuel, 2022, 317: 123556.

Nishizawa, Y., Uchida, M., Watanabe, N., et al. Deformation behavior of microparticle-based polymer films visualized by afm equipped with a stretching device. ACS Applied Materials & Interfaces, 2024, 16(45): 63073-63082.

Pan, H., Hu, Y., Liu, H., et al. Thermal damage mechanism and micro-mechanical property analysis of carbonate rocks under laser irradiation. Rock Mechanics and Rock Engineering, 2024, 58: 3437-3459.

Penedo, M., Miyazawa, K., Okano, N., et al. Visualizing intracellular nanostructures of living cells by nanoendoscopy-AFM. Science Advances, 2021, 7(52): eabj4990.

Saeedi, B., Vatankhah, R., Moghaddam, V. A. Analytical solution for size-dependent nonlinear behavior of AFM microcantilever with assembled probe in liquid environments. Mechanics of Advanced Materials and Structures, 2024, 31(27): 8948-8965.

Sevostianov, I., Vernik, L. Micromechanics-based rock-physics model for inorganic shale. Geophysics, 2021, 86(2): MR105-MR116.

Tang, X. Nanomechanics of coal: A case study of Pocahontas coal. Coal Science and Technology，2020，48(2): 220-229.

Teng, S., Liu, A., Situ, Z., et al. Plug-and-play method for segmenting concrete bridge cracks using the segment anything model with a fractal dimension matrix prompt. Automation in Construction, 2025, 170: 105906-105906.

Volkov, D. S., Rogova, O. B., Proskurnin, M. A. Photoacoustic and photothermal methods in spectroscopy and characterization of soils and soil organic matter. Photoacoustics, 2020, 17: 100151.

Wang, K., Taylor, K. G., Ma, L. Advancing the application of atomic force microscopy (AFM) to the characterization and quantification of geological material properties. International Journal of Coal Geology, 2021, 247: 103852.

Wang, M., Liu, L. Investigation of microscale aging behavior of asphalt binders using atomic force

Sustain. Earth Resour. Commun. 2025, 1(1): 4-17

16

microscopy. Construction and Building Materials, 2017, 135: 411-419.

Wang, Q., Wang, T., Zhong, P., et al. Study of the surface pore structure and micromechanical properties of the Longmaxi shale. Petroleum Science Bulletin, 2023, 8(5): 626-636.

Wang, S., Wang, L., Ren, B., et al. Mechanical behavior and fracture characteristics of high-temperature sandstone under true triaxial loading conditions. Journal of Materials Research and Technology, 2024, 28569-28581.

Wei, X., Jia, L., Duan, B., et al. Recent progress and applications of NanoIR-AFM in morphological characterization of organic solar cells. Advanced Functional Materials, 2024, 34(49): 2408960.

Wu, J., Liu, H., Wei, P., et al. Effect of shot peening coverage on residual stress and surface roughness of 18CrNiMo7-6 steel. International Journal of Mechanical Sciences, 2020, 183: 105785.

Wu, J., Lu, Y., Wang, K., et al. Combined effects of freeze–thaw cycles and chemical corrosion on triaxial mechanical properties of sandstone. Geomechanics and Geophysics for Geo-Energy and Geo-Resources, 2023, 9: 57.

Xie, H., Li, X. Microstructure and nanomechanical characterization of tectonic coal based on SEM, AFM, XRD and DSI. Surfaces and Interfaces, 2024, 46: 104158.

Yang, L., Yang, D., Li, Y., et al. Nanoindentation study on microscopic mineral mechanics and bedding characteristics of continental shales. Energy, 2024, 312: 133614.

Yang, Y. L., Meng, Z. D., Wang, H. L., et al. Taking photoacoustic force into account in liquid-phase peak force infrared microscopy. The Journal of Physical Chemistry Letters, 2024, 15(32): 8233-8239.

Yu, T., Liu, H., Wang, M. Study on enhancement mechanism of asphalt microstructure by graphene/graphene oxide based on MD and AFM. Surfaces and Interfaces, 2024, 55: 105468-105468.

Zhang, E., Shan, L., Qi, X., et al. Investigating the relationship between chemical composition and mechanical properties of asphalt binders using atomic force microscopy (AFM). Construction and Building Materials, 2022, 343: 128001.

Zhang, H., Wang, Y., Yu, T., et al. Microstructural characteristics of differently aged asphalt samples based on atomic force microscopy (AFM). Construction and Building Materials, 2020, 255: 119388.

Zhang, M., Xu, J., Jiang, Q., et al. Cross-scale characterization of the Young's modulus of slate using atomic force microscopy. Rock and Soil Mechanics, 2022, 43(S1): 245-257.

Zhang, Z., Li, C., Ning, F., et al. Pore fractal characteristics of hydrate-bearing sands and implications to the saturated water permeability. Journal of Geophysical Research: Solid Earth, 2020, 125(3): e2019JB018721.

Zhou, Y., Lv, W., Li, B., et al. A realistic 3D grain-based modeling approach for reproducing the mechanical and failure behavior of brittle granites. International Journal of Rock Mechanics and Mining Sciences, 2025, 185: 105981-105981.

Zhu, Q., Shao, J. Micromechanics of rock damage: Advances in the quasi-brittle field. Journal of Rock Mechanics and Geotechnical Engineering, 2017, 9(1): 29-40.